J Mater Sci: Mater Electron (2022) 33:25920–25929

The structure, vacancy characteristics, and magnetic and dielectric properties of $GdMn_{1-x}W_xO_3$ ceramics

Tao Li[1], Haizeng Liu[1], Jing Chen[1], Dewei Liu[1], and Haiyang Dai[1,*]

[1] School of Physics and Electronic Engineering, Zhengzhou University of Light Industry, Zhengzhou 450002, China

Received: 20 July 2022
Accepted: 3 October 2022
Published online: 17 October 2022

ABSTRACT

The effects of W^{6+} ion substitution at the Mn site on the structure, vacancy characteristics, and magnetic and dielectric properties of $GdMnO_3$ ceramics synthesized using the solid-state method were investigated. Structural measurements indicate that all $GdMn_{1-x}W_xO_3$ ceramics exhibit a single-phase structure, and that the introduction of W^{6+} ions induces structural distortion. W^{6+} substitution changes the valence states of Mn and the oxygen vacancy concentration in $GdMn_{1-x}W_xO_3$. Experimental results of positron annihilation indicate that the concentration of cation vacancies increases with increasing W^{6+} concentration. The evolution of temperature- and magnetic field-dependent magnetization curves indicates that appropriate W^{6+} substitution could evidently improve the magnetization of $GdMn_{1-x}W_xO_3$. Dielectric measurements reveal that the W^{6+}-substituted samples exhibit giant dielectric characteristics over a broad frequency range. It was found that the magnetization of $GdMn_{1-x}W_xO_3$ has a close relationship with vacancy concentration, structural distortion, and the dilution effect. Further, the giant dielectric constant behavior of $GdMn_{1-x}W_xO_3$ ceramics is related to the mixed-valent structure of Mn and the resistivity of grain and grain boundary.

1 Introduction

$GdMnO_3$ (GMO) is a typical single-phase multiferroic material with a distorted orthorhombic perovskite structure, which has attracted worldwide attention owing to its special magnetic and ferroelectric structure, and intrinsically strong magnetoelectric coupling [1–4]. As temperature decreases, GMO shows multiple magnetic transitions owing to the interactions of Mn–Mn, Gd–Gd, and Mn–Gd. It is found that GMO transitions from the paramagnetic to the antiferromagnetic phase at ~ 43 K, followed by a weak ferromagnetic transition at ~ 25 K. A ferroelectric state appears below 25 K owing to the spin canting of Mn^{3+} and Gd^{3+} moments [5, 6]. Although the electric and magnetic properties of GMO have been investigated by researchers, the physical mechanism of ferroelectricity generation and complex spin states is still unclear, and the electric and magnetic transition temperature is relatively low.

Recently, various methods have been employed to comprehend the origin of physical properties and

Address correspondence to E-mail: haiyangdai@163.com

https://doi.org/10.1007/s10854-022-09282-7

enhance the properties of GMO material, such as (1) synthesizing GMO with a novel method [7, 8]; (2) applying external pressures to GMO systems [9]; (3) substituting the Gd site with Y^{3+}, Sr^{2+}, etc., or replacing the Mn site with Fe^{3+}, Cr^{3+}, etc. [10–13]; (4) introducing cationic vacancies in the crystal lattice [14]; (5) synthesizing GMO nanoparticles [15]; and (6) depositing a GMO film [16]. Among these, ion substitution is an efficient method to modulate the structure and performances of GMO. The Ho^{3+}-substituted $Gd_{1-x}Ho_xMnO_3$ has been investigated by Zhang et al. [17], who showed that Ho substitution induced a decrease in Mn–O–Mn bond angle and, hence, improved electric polarization. Tiwari et al. [13] explored the influences of Cr substitution on the structure and magnetic performances of $GdMn_{1-x}Cr_xO_3$, and found that Cr doping induced a structural transformation and a decrease of Jahn–Teller distortion. Further, an increase in the magnetic transition temperature along with magnetization reversal with spin reorientation and magnetic switching was observed in Cr-doped GMO owing to the magnetic interactions between Gd^{3+}, Mn^{3+}, and Cr^{3+} ions. Herein, the W^{6+} ion is selected as a dopant owing to its similar ionic radius to Gd^{3+} [18], and its potential effects on the structural, magnetic, and dielectric properties of GMO.

Vacancy defects can observably influence the electric and magnetic performances of perovskite oxide materials [19]. Therefore, probing the evolution of vacancy characteristics in perovskite oxides is beneficial for exploring inherent physical mechanisms and improving the performances of perovskite oxides. Positron annihilation technology is often used to investigate the vacancies information in material due to its high sensitivity to atomic scale defects [20, 21]. Unfortunately, research on the vacancies characteristics of GMO systems investigated using positron annihilation technology is still lacking. Therefore, using positron annihilation technology to detect vacancy and reveals vacancy evolution in the performance of GMO will be extremely helpful for fundamental research and material applications. Herein, the $GdMn_{1-x}W_xO_3$ multiferroic samples were prepared using the solid-state method, and the vacancy information in $GdMn_{1-x}W_xO_3$ compounds was characterized using the positron annihilation technology. The influence of W^{6+} ion replacement on the structural, vacancy, and magnetic and dielectric performance of $GdMn_{1-x}W_xO_3$ samples was studied.

2 Experimental details

The $GdMn_{1-x}W_xO_3$ (x = 0.00–0.20) ceramics were synthesized using the solid-state synthesis method with Gd_2O_3 (4 N), Mn_3O_4 (4 N), and WO_3 (4 N) precursors. The starting materials with stoichiometric ratio were mixed and thoroughly ground using an agate mortar to form a homogeneous mixture. The mixtures were calcined in air at 1273 K for 24 h followed by several intermittent grindings for 2 h and then calcined in air again at 1523 K for 24 h. Finally, the calcined mixtures were pressed into cylindrical pellets under 10 MPa and sintered in air at 1623 K for 24 h.

The structural details of the $GdMn_{1-x}W_xO_3$ samples were collected using a Brucker D8 Advance X-ray diffractometer (CuKα radiation). The valence states of the specimens were analyzed using X-ray photoelectron spectroscopy (XPS, XSAM800) at room temperature. Raman experiments were conducted using a Renishaw inVia Raman spectrometer using an excitation wavelength of 532 nm. The microstructural characterization of $GdMn_{1-x}W_xO_3$ ceramics was detected using a Quanta 250 FEG scanning electron microscope (SEM). The positron annihilation spectroscopy data were collected using a fast-low coincidence system at ~ 298 K. The positron annihilation data could be obtained using the LT 9.0 program. Magnetic measurements between − 5 and 5 kOe were performed using a SQUID magnetometer (Quantum Design, USA) over a temperature range of 5–300 K. The dielectric properties and impedance spectrum of the ceramics were recorded with an Agilent HP 4194 A impedance analyzer in the 100–1 × 10^7 Hz frequency range.

3 Results and discussion

The X-ray diffraction (XRD) patterns of $GdMn_{1-x}W_xO_3$ samples are shown in Fig. 1. The peaks of $GdMn_{1-x}W_xO_3$ samples can be indexed by orthorhombic crystal structures with the space group *Pbnm*. This means that the substitution of the W^{6+} ion at the Mn site does not change the crystal structure of GMO. No secondary phases can be detected in the $GdMn_{1-x}W_xO_3$ compounds under XRD resolution, confirming the successful preparation of $GdMn_{1-x}W_xO_3$ with a single-phase structure using the solid-state synthesis method. The expansion of XRD patterns in the

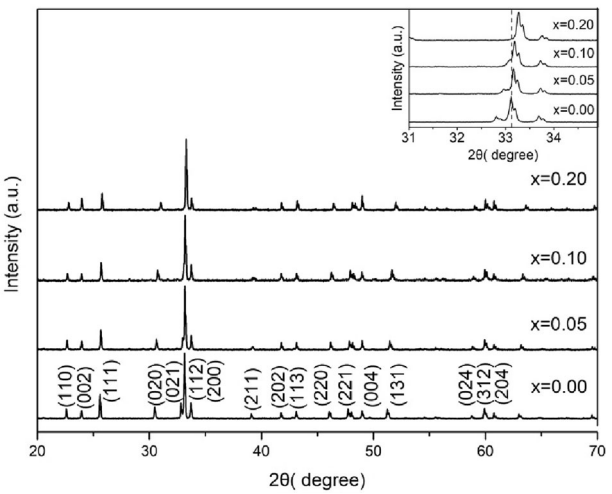

Fig. 1 X-ray diffraction (XRD) patterns of $GdMn_{1-x}W_xO_3$ samples. The inset represents the expanded (112) peak

vicinity of $2\theta = 33.1°$ for $GdMn_{1-x}W_xO_3$ ceramics is shown in the inset of Fig. 1. The peak position of 112 for $GdMn_{1-x}W_xO_3$ gradually shifts to higher 2θ angles as the substitution of W^{6+} ions increases, indicating that the W^{6+} ion has successfully replaced the Mn ion in GMO, causing lattice distortion. The above phenomena could be attributed to the radius of W^{6+} ion (0.060 Å) being smaller than that of the Mn^{3+} ion (0.0645 Å) [18].

To understand the charge compensation induced by W^{6+} substitution, the element valence states and content in the $GdMn_{1-x}W_xO_3$ samples were analyzed using XPS. Figure 2a shows the core-level XPS spectra of Mn $2p_{3/2}$ for $GdMn_{1-x}W_xO_3$ compounds. The symmetrical Mn $2p_{3/2}$ band for the unsubstituted GMO implies that only Mn^{3+} is present in the unsubstituted sample, while the asymmetrical Mn $2p_{3/2}$ spectra for the W^{6+}-substituted GMO indicate that Mn exists in several oxidation states in the W^{6+}-substituted samples. It has been reported that the binding energy of Mn^{2+} and Mn^{3+} in the Mn $2p_{3/2}$ XPS spectrum is located at ~ 640.0 eV and ~ 642.2 eV, respectively [14]. Therefore, the first deconvoluted peak in W^{6+}-substituted ceramics is attributed to Mn^{2+} (red line), and the other deconvoluted peak corresponds to Mn^{3+} (blue line). The Mn^{2+} concentration can be obtained using the following formula:

$$[Mn^{2+}] = A(Mn^{2+})/A(Mn^{2+} + Mn^{3+}), \quad (1)$$

where A is the corresponding peak area. The Mn^{2+} concentration in the $GdMn_{0.95}W_{0.05}O_3$, $GdMn_{0.90}W_{0.10}O_3$, and $GdMn_{0.80}W_{0.20}O_3$ samples is ~ 10.0%, 21.8%, and 22.5%, respectively. This means that a certain amount of W^{6+} substitution introduces more Mn^{2+} in $GdMn_{1-x}W_xO_3$ samples, while the Mn^{2+} content remains unchanged when x is higher than 0.10. The charge compensation induced by the addition of W^{6+} ions to GMO at the Mn site may be realized by the conversion of Mn^{3+} to Mn^{2+}. Therefore, W^{6+} substitution could increase Mn^{2+} concentration. Figure 2b depicts the O 1 s XPS spectra for $GdMn_{1-x}W_xO_3$ samples. Each spectrum of O 1 s can be deconvoluted into two components: the low binding energy component (O_I) at ~ 529.5 eV, attributed to the oxygen ion in the crystal structure, and the higher one (O_{II}) at ~ 531.6 eV that corresponds to oxygen vacancies [22]. The ratio of O_{II}/O_I is ~ 0.352, 0.311, 0.306, and 0.185 for the unsubstituted GMO, $GdMn_{0.95}W_{0.05}O_3$, $GdMn_{0.90}W_{0.10}O_3$, and $GdMn_{0.80}W_{0.20}O_3$ samples, respectively. This indicates that the oxygen vacancy content is roughly the same in samples with x values between 0.00 and 0.10, it decreases for the $x = 0.20$ sample. Charge compensation induced by the addition of W^{6+} ions to GMO at the Mn site may be realized by a decrease in cation valency (i.e., the formation of Mn^{2+}) and/or anion vacancies. Therefore, W^{6+} ion substitution can modulate the valence state of Mn ions and the concentration of oxygen vacancies. The change of Mn^{2+} ions and oxygen vacancy concentrations demonstrates that the predominant charge compensation mechanism in $GdMn_{0.95}W_{0.05}O_3$ and $GdMn_{0.90}W_{0.10}O_3$ samples is the conversion of Mn^{3+} to Mn^{2+}, while the conversion of Mn^{3+} to Mn^{2+} and the elimination of oxygen vacancies are found to be the dominant charge compensation mechanism in $GdMn_{0.80}W_{0.20}O_3$ sample.

Figure 3 shows the SEM images of the unsubstituted and W^{6+}-substituted GMO compounds. The prepared ceramics exhibit a dense microstructure with plump, irregular hexagonal grains, and clear grain boundaries. The grain size of all the samples is not uniformly distributed. The grain size for the $GdMn_{0.95}W_{0.05}O_3$ and $GdMn_{0.90}W_{0.10}O_3$ samples is similar to that of the unsubstituted GMO; it becomes smaller for the $x = 0.20$ samples. This indicates that a larger concentration of W^{6+} substitution could hinder the grain growth of GMO. This may be related to the decrease in the oxygen vacancy concentration caused by W^{6+} substitution, which results in the slower

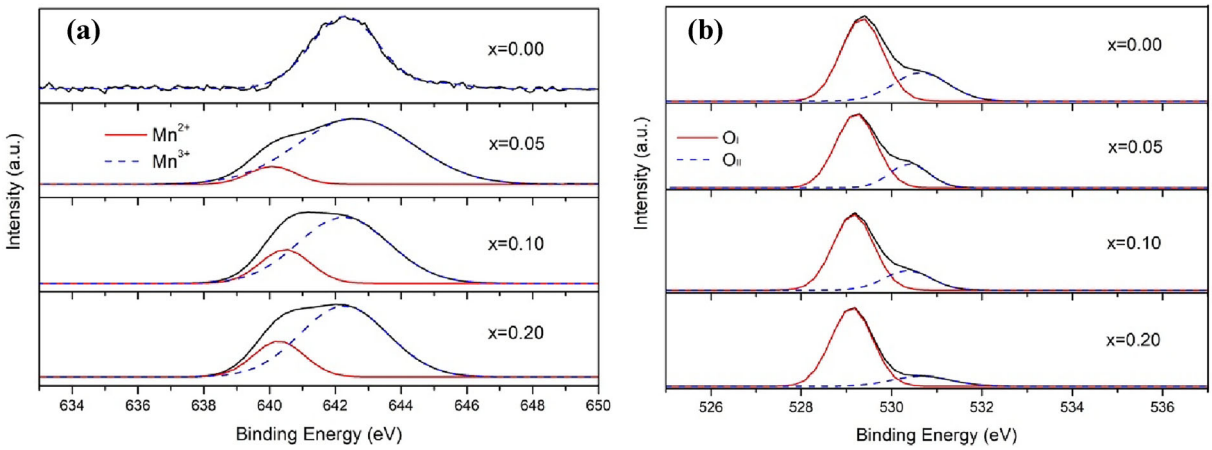

Fig. 2 The deconvolution Mn 2p3/2 (**a**) and O1s (**b**) X-ray photoelectron spectroscopy (XPS) spectra of $GdMn_{1-x}W_xO_3$ ceramics

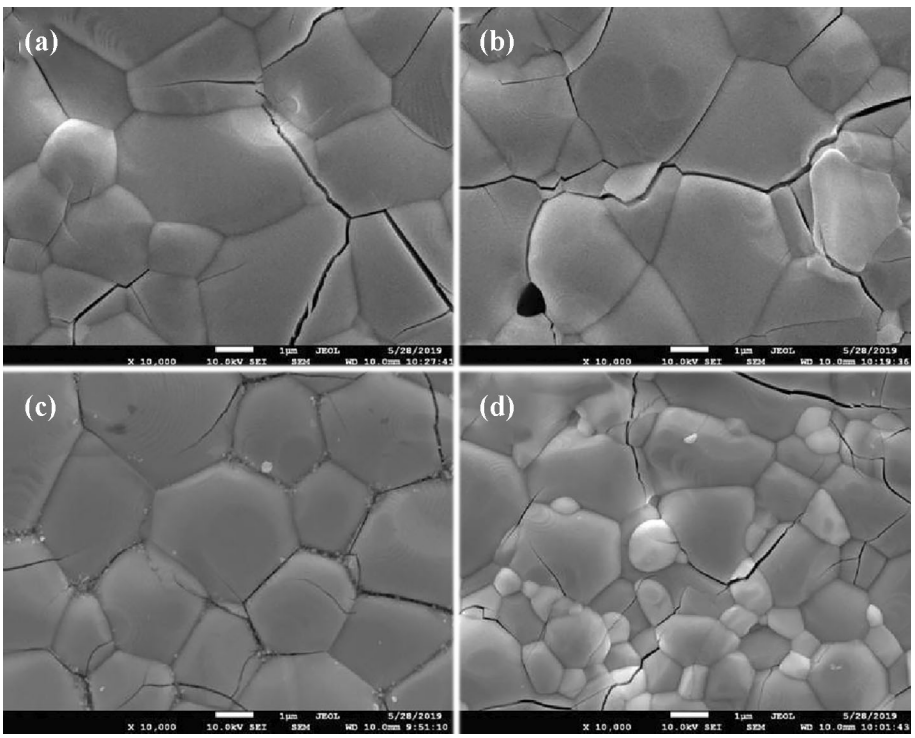

Fig. 3 SEM images of the $GdMn_{1-x}W_xO_3$ compounds: **a** $x = 0.00$, **b** $x = 0.05$, **c** $x = 0.15$, **d** $x = 0.20$

movement of oxygen ions and, hence, inhibits the grain growth rate [23].

Positron annihilation lifetime spectrum measurement was performed to investigate the defects information in the $GdMn_{1-x}W_xO_3$ samples. The fitted positron annihilation lifetime spectrum comprises three lifetime components τ_1, τ_2, and τ_3 with relative intensities I_1, I_2, and I_3 ($I_1 + I_2 + I_3 = 1$), respectively. The longest lifetime τ_3 ($\sim$ 1200 ps) is considered to be the result of positrons annihilated at the grain surface of GMO-based ceramics [24–26]. Owing to the lower intensity ($I_3 < 0.8\%$), τ_3 and I_3 are neglected herein, while I_1 and I_2 are renormalized. The values of the positron parameters τ_1, τ_2, I_2, and τ_{av} in $GdMn_{1-x}W_xO_3$ ceramics are shown in Fig. 4; τ_1 is the reduced bulk positron lifetime, which is attributed to the annihilation of positrons in the perfect lattice; τ_2 is mainly related to the lifetime of positrons annihilated at vacancy type defects within the samples, representing the information of defect size [24–29]. The intensity I_2 is the probability of positrons annihilated at the localized defect state, which reflects the defect concentration in the experimental materials. As shown in Fig. 4, τ_2 increases for $x = 0.00$–0.10 and

then decreases. Because a higher value of τ_2 represents a bigger size of vacancy in solid materials, the change in τ_2 indicates that the vacancy size increases for the x = 0.00–0.10 samples, while it decreases with further increase in the W^{6+} content. The intensity I_2 increases monotonously as the W^{6+} content x increases. This suggests that W^{6+} replacement can introduce considerable cation vacancy defects in $GdMn_{1-x}W_xO_3$, and that the vacancy concentration increases with increasing W^{6+} content. The substitution of W^{6+} ion for Mn^{3+} in GMO causes the structural distortion, which might introduce cation vacancies in $GdMn_{1-x}W_xO_3$. Furthermore, on substituting Mn^{3+} with W^{6+} ions, cationic vacancy defects with a negative charge are created owing to charge compensation, which can be described by Eq. (2):

$$WO_3 \rightarrow W_{Mn}^{\bullet\bullet\bullet} + V_{Mn}''' + 3O. \quad (2)$$

The above two factors induce the increase of cationic vacancy concentration in W^{6+}-substituted ceramics. The average lifetime τ_{av} can also be used to judge the defect characteristics in a solid, which can be expressed by the following formula [28, 29]:

$$\tau_{av} = \tau_1 \cdot I_1 + \tau_2 \cdot I_2. \quad (3)$$

It can be found from Fig. 4 that the change of τ_{av} with W^{6+} concentration x has the similar trend as that of I_2. Therefore, the correlation between vacancies concentration and W^{6+} substitution content is further verified by the change of τ_{av}.

The temperature dependence of magnetization (M-T) for $GdMn_{1-x}W_xO_3$ ceramics measured under zero-field-cooled (ZFC) and field-cooled (FC) modes at 1 kOe is displayed in Fig. 5. According to previous literature [8, 30], GMO undergoes three magnetic transitions at low temperature, namely, paramagnetism to antiferromagnetism at ~ 43 K attributed to the appearance of Mn^{3+} AFM ordering, antiferromagnetism to ferromagnetism at 25 K resulting from the canted AFM of Mn^{3+}, and ferromagnetism to antiferromagnetism at 8 K owing to Gd^{3+} AFM ordering. The ZFC and FC plots shown in Fig. 5 are almost equal in the temperature range of 300–50 K for $GdMn_{1-x}W_xO_3$ samples; however, the magnetic transition at ~ 43 K disappears in $GdMn_{1-x}W_xO_3$ owing to the strong paramagnetic moment of Gd. For the x = 0.00–0.10 ceramics, a remarkable improvement of magnetization in the ZFC curve at ~ 23 K marks the onset of ferromagnetic ordering, then the magnetic transition at ~ 8 K appears, and finally magnetization increases with a decrease in temperature. For the $GdMn_{0.80}W_{0.20}O_3$ samples, a magnetic transition at ~ 8 K in the ZFC curve cannot be observed, which may shift to a lower temperature. After a field cooling measurement, the magnetization for $GdMn_{1-x}W_xO_3$ increases with a decrease in temperature, while the magnetic transition at ~ 8 K in the ZFC curves disappears owing to the enhancement of the local magnetic field at Gd, which can be attributed to the ferromagnetic ordering of the Mn moment. To study the magnetic interactions in $GdMn_{1-x}W_xO_3$, the temperature dependence of inverse susceptibility ($1/\chi$–T) for all samples is displayed in the illustration in Fig. 5. All $1/\chi$–T curves obey the Curie–Weiss law at a higher temperature, and the calculated Curie–Weiss temperature (T_{cw}) for $GdMn_{1-x}W_xO_3$ samples is negative, indicating that antiferromagnetic interaction is predominant in $GdMn_{1-x}W_xO_3$ compounds.

Figure 6 depicts the magnetic field dependence of the magnetization (M-H) for $GdMn_{1-x}W_xO_3$ ceramics measured at 5 K, 30 K, and 40 K. The M-H curves for $GdMn_{1-x}W_xO_3$ samples recorded at 30 K and 40 K exhibit linear characteristics, indicating antiferromagnetic behavior; meanwhile, the curve measured at 5 K shows non-linear characteristics, demonstrating that weak ferromagnetic/ferrimagnetic behavior is presented. The presence of weak ferromagnetism/ferrimagnetism at 5 K should be the result of canted Gd and Mn moments [31, 32]. The M–H loops for $GdMn_{1-x}W_xO_3$ samples at low temperatures are unsaturated demonstrating the coexistence of antiferromagnetic and weak ferromagnetic/ferrimagnetic properties in

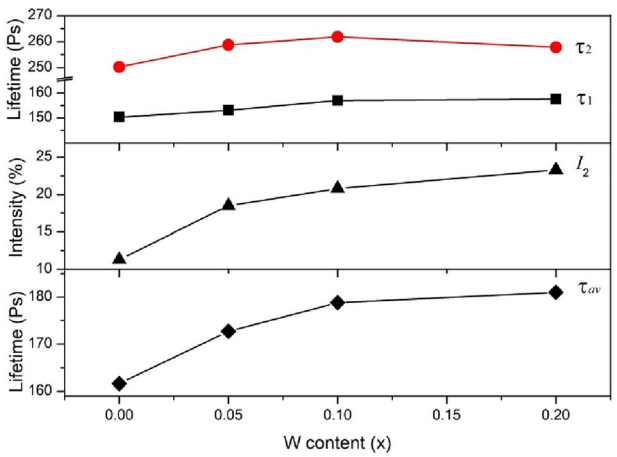

Fig. 4 Variations in the positron lifetimes τ_1, τ_2, τ_{av}, and I_2 in the $GdMn_{1-x}W_xO_3$ samples

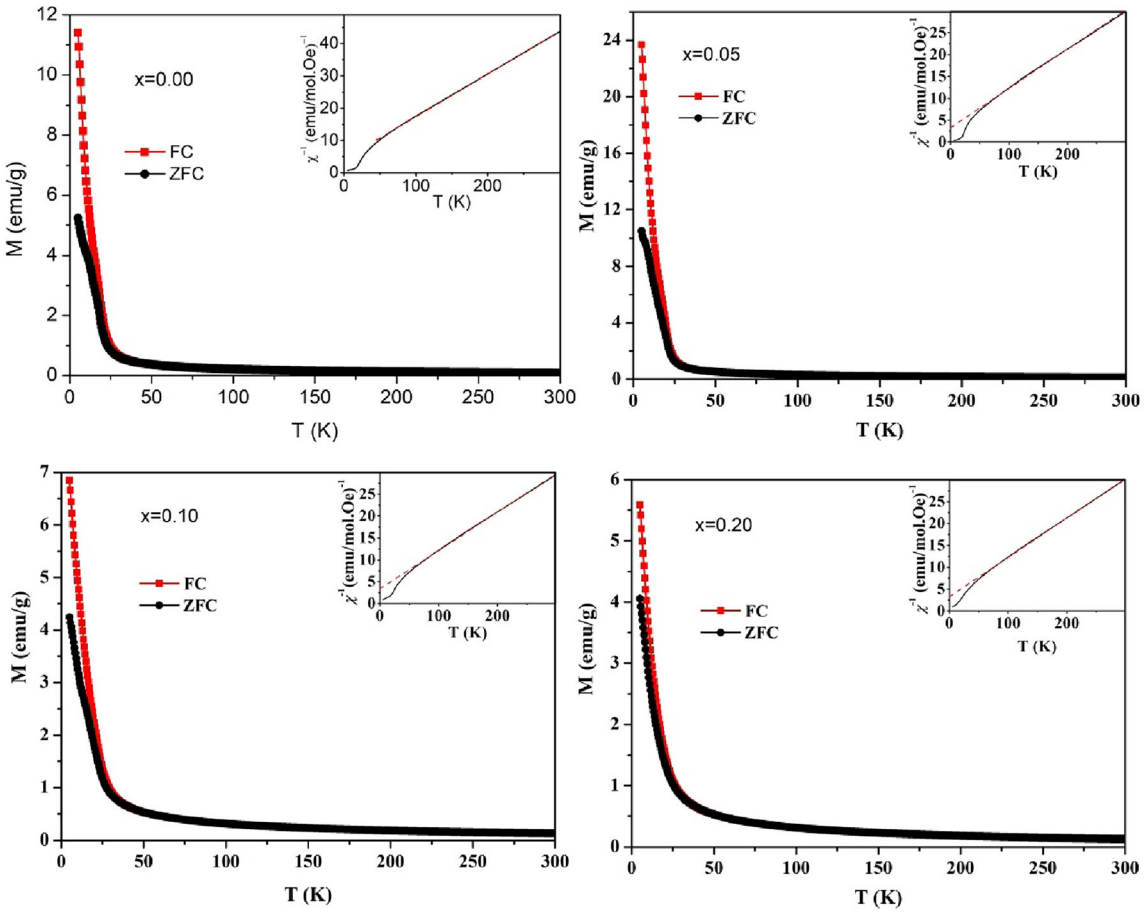

Fig. 5 Temperature dependence of the zero-field-cooled (ZFC) and field-cooled (FC) magnetization curves for the $GdMn_{1-x}W_xO_3$ samples

the prepared compounds. The remnant magnetization (*M*r) at 5 K is ~ 7.38, 18.25, 3.18, and 2.95 emu/g for unsubstituted GMO, $GdMn_{0.95}W_{0.05}O_3$, $GdMn_{0.90}W_{0.10}O_3$, and $GdMn_{0.80}W_{0.20}O_3$, respectively. It can be observed that *M*r initially increases with increasing W^{6+} amount from 0.00 to 0.05 but decreases as the W^{6+} content increases from 0.05 to 0.20. It can be observed from Fig. 6 that $GdMn_{1-x}W_xO_3$ ceramics show ferromagnetic/ferrimagnetic properties at 5 K, and the insertion of cationic vacancies in ferromagnetic/ferrimagnetic orderings would improve magnetization. Meanwhile, GMO exhibits a spiral spin magnetic structure at low temperatures; the structural distortion caused by W^{6+} substitution could suppress the magnetic spiral spin and increase magnetization. Therefore, the magnetization increases with increasing W^{6+} content *x* from 0.00 to 0.05. The substitution of nonmagnetic W^{6+} ions will cause magnetic dilution and thus a decrease in magnetization [33]. Therefore, magnetization decreases with increasing *x* from 0.05 to 0.20. Moreover, the change in the lattice structure, and the interaction of the Mn^{3+}–Mn^{4+}, Gd^{3+}–Mn^{3+}/Mn^{4+}, and Gd^{3+}–Gd^{3+} induced by W^{6+} substitution also affect the magnetic behavior of the GMO system [8, 14, 30].

The electrical properties of the grains and the grain boundaries of all the samples were investigated using impedance spectroscopy. The impedance plots (Z* plots, Z″ vs. Z′) for $GdMn_{1-x}W_xO_3$ ceramics at room temperature are shown in Fig. 7, and the expended view of high-frequency data close to the origin for $GdMn_{1-x}W_xO_3$ ceramics is illustrated in Fig. 7. The grain resistance (R_g) and grain boundary resistance (R_{gb}) can generally be determined from the diameter of two semicircular arcs observed from the impedance spectrum at high- and low-frequency ranges, respectively [34]. The nonzero intercept on the Z′ axis presents the resistance value of the grains. Further, the resistance value of grain boundary can be directly obtained by the other intercept on the Z′ axis from the low-frequency impedance data [34]. It can be seen from Fig. 7 that only a part of the grain boundary

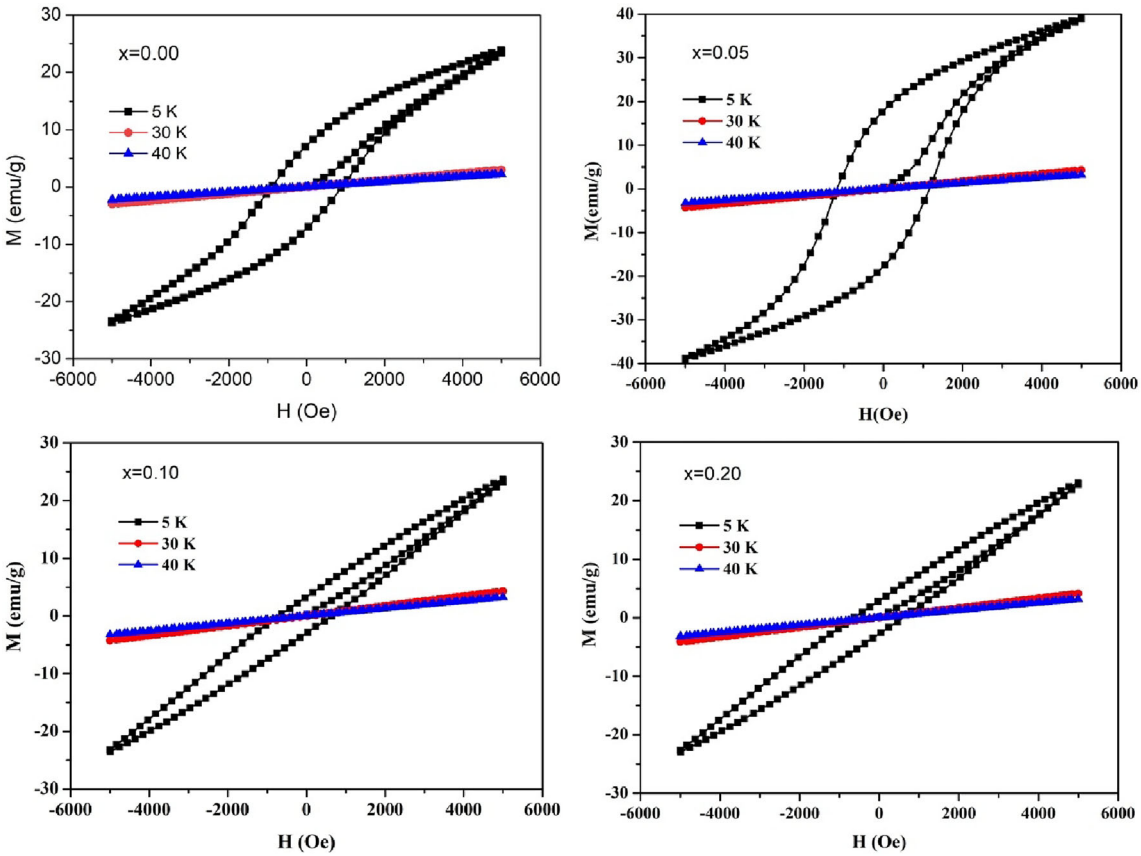

Fig. 6 Field-dependent magnetization (M–H) curves of the $GdMn_{1-x}W_xO_3$ samples measured at 5 K, 30 K, and 40 K

semicircles or arcs is observed because of the limit of the measured frequency range. The nonzero intercept of the large arc at high frequencies is ~ 62, 80, 88, and 303 kΩ.cm corresponding to x = 0.00, 0.05, 0.10, and 0.20 samples, respectively. This means that the value of R_g changes little as the concentration of W^{6+} increases from 0.00 to 0.10; however, R_g for the x = 0.20 sample is clearly greater than that of the other samples. Although the R_{gb} of the samples cannot be obtained due to the nonzero intercept of large arc at low frequencies, it can be inferred that the values of R_{gb} increase with increasing W^{6+} substitution concentration according to the curvature of circular arcs. Therefore, W^{6+} substitution can improve the resistivity of grain and grain boundary.

Figure 8 displays the variation of dielectric constant (ε_r) with frequency at room temperature for the $GdMn_{1-x}W_xO_3$ samples. ε_r for all these samples exhibits the same increasing trend with increasing frequency; it decreases considerably in the low-frequency range ($< 10^4$) and remains almost constant as the frequency exceeds 10^4. This phenomenon may be related

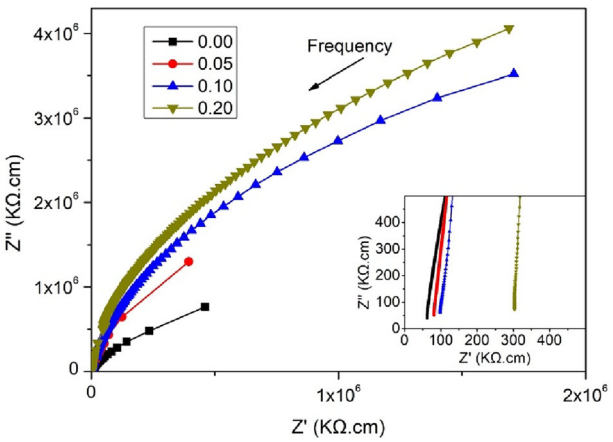

Fig. 7 Impedance complex plane plots for $GdMn_{1-x}W_xO_3$ samples

to the relaxation of space charge polarization, which cannot keep up with the change of frequency at high frequencies. From Fig. 8, it can be clearly seen that the value of ε_r is enhanced considerably by W^{6+} ion substitution in the high-frequency range, which is ~ 125.8, 8369.7, 9216.1, and 11,023.2 measured at

1×10^7 Hz for unsubstituted GMO, $GdMn_{0.95}W_{0.05}O_3$, $GdMn_{0.90}W_{0.10}O_3$, and $GdMn_{0.80}W_{0.20}O_3$, respectively. This shows that W^{6+} ion substitution makes the material display giant dielectric properties. Till date, few studies have reported the giant dielectric constant of this material at higher frequencies, and thus, the mechanism of giant dielectric properties remains unknown. In the typical giant dielectric $CaCu_3Ti_4O_{12}$ ceramics, the polar arrangement of electrons on mixed-valence Ti^{3+}/Ti^{4+} and/or Cu^{+}/Cu^{2+} is the physical origin of giant dielectric behavior [35]. The giant dielectric response in $LuFe_2O_4$ ceramics also supports this mechanism [36]. The XPS results in Fig. 2 demonstrate that the mixed valence of Mn^{2+}/Mn^{3+} exists in the W^{6+}-substituted GMO. Therefore, the giant dielectric properties of $GdMn_{1-x}W_xO_3$ may be related to the polar arrangement of electrons on the mixed-valence structure of Mn^{2+}/Mn^{3+}. Meanwhile, grain and grain boundary having large resistivity are conducive to the improvement of the dielectric constant. The results of impedance spectroscopy show that W^{6+} substitution can improve the resistivity of grain and grain boundary, so W^{6+} substitution enhances the dielectric constant of GMO. Therefore, the formation mechanism of the giant dielectric properties in $GdMn_{1-x}W_xO_3$ may have risen from the polar arrangement of electrons in the mixed-valence structure of Mn^{2+}/Mn^{3+} and the increase in grain and grain boundary resistivity induced by W^{6+} substitution. The room-temperature dielectric loss (tan δ) as a function of frequency for $GdMn_{1-x}W_xO_3$ ceramics is shown in Fig. 9. The change of tan δ with frequency shows a similar trend to that of the dielectric constant. tan δ for unsubstituted GMO, $GdMn_{0.95}W_{0.05}O_3$, and $GdMn_{0.90}W_{0.10}O_3$ samples is almost the same, while $GdMn_{0.80}W_{0.20}O_3$ samples have a lower dielectric loss than that of other samples, which may be related to the leakage current in the prepared ceramics. As shown in Fig. 2, the concentration of oxygen vacancy in the $GdMn_{0.80}W_{0.20}O_3$ sample is lower than that of other samples, which will decrease electronic conduction in the material and, thus, considerably influence the electronic properties of $GdMn_{1-x}W_xO_3$ [37]. Therefore, tan δ of $GdMn_{0.80}W_{0.20}O_3$ is lower than that of other samples.

4 Conclusion

The structural characterstics and magnetic and dielectric performance of $GdMn_{1-x}W_xO_3$ polycrystalline ceramics synthesized using the solid-state reaction method were studied. The substitution of W^{6+} at the Gd site induces structural distortion. W^{6+} ion substitution induces the conversion of Mn^{3+} to Mn^{2+} and the elimination of oxygen vacancies in $GdMn_{1-x}W_xO_3$. The positron annihilation studies reveal that W^{6+} ion substitution can change the cation vacancy size and that the vacancy concentration increases with an increasing amount of W^{6+} ions. *M–T* curves show that antiferromagnetic interaction is dominant in $GdMn_{1-x}W_xO_3$ samples. *M-H* curves show that all samples display weak ferromagnetic/ferrimagnetic behavior at 5 K, and the $GdMn_{0.95}W_{0.05}O_3$ sample shows optimized magnetic properties. Furthermore, the W^{6+}-substituted samples exhibit giant dielectric characteristics over a

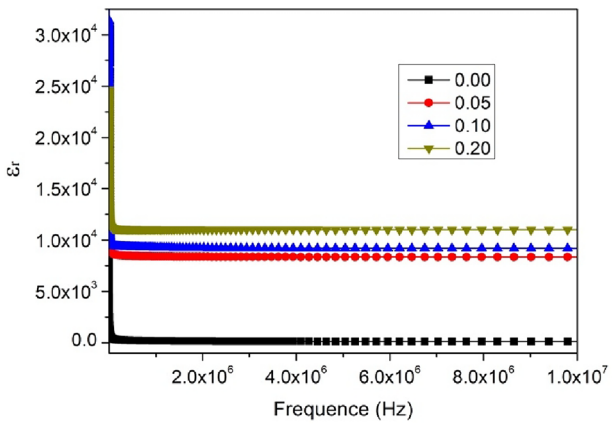

Fig. 8 Frequency dependence of dielectric constant for $GdMn_{1-x}W_xO_3$ samples at room temperature

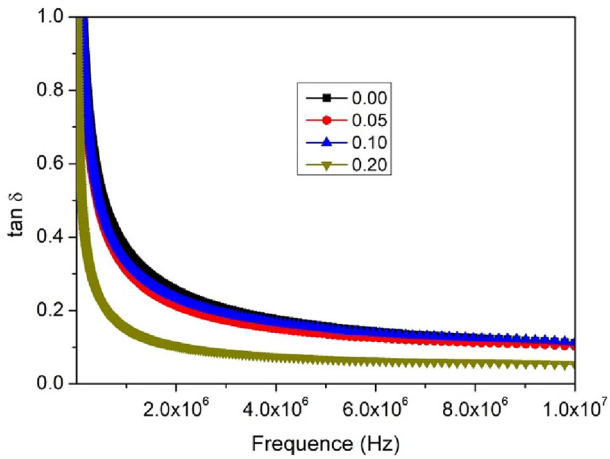

Fig. 9 Frequency dependence of dielectric loss for $GdMn_{1-x}W_xO_3$ samples at room temperature

broad frequency range. The above results suggest that the magnetic properties of the $GdMnO_3$ system are mainly modulated by vacancy concentration, structural distortion, and the magnetic dilution effect; the mixed-valence structure of Mn^{2+}/Mn^{3+} and the increase in grain and grain boundary resistivity are the main factors in the appearance of giant dielectric properties. Present findings show that the physical properties of $GdMnO_3$ materials can be tailored by W^{6+} substitution.

Acknowledgements

This work is supported by the National Natural Science Foundation of China (Grant Nos. 12275242, 11975211, and 12005194), and the Natural Science Foundation of Henan Province (Grant Nos. 212300410092, 212102210489).

Author contributions

TL contributed to material preparation, investigation, and writing-original draft; HL contributed to material preparation, data collection, and validation; JC contributed to validation and analysis; DL contributed to formal analysis and validation; and HD contributed to resources, conceptualization, investigation, and writing-original draft. All authors read and approved the final manuscript.

Funding

This work is supported by the National Natural Science Foundation of China (Grant Nos. 12275242, 11975211, and 12005194), and the Natural Science Foundation of Henan Province (Grant Nos. 212300410092, 212102210489).

Data availability

The datasets generated during and/or analyzed during the current study are available from the corresponding author on reasonable request.

Declarations

Conflict of interest There is no conflict of interest to declare.

References

1. J. Stein, M. Baum, S. Holbein, T. Finger, T. Cronert, C. Tolzer, T. Frohlich, S. Biesenkamp, K. Schmalzl, P. Steffens, C.H. Lee, M. Braden, Phys. Rev. Lett. **119**, 177201 (2017)
2. P.J. Xue, H. Wu, Y. Lu, X.H. Zhu, J. Mater. Sci. Technol. **34**, 914 (2018)
3. C. Chakrabarti, Q.S. Fu, X.H. Chen, Y. Qiu, S.L. Yuan, C.L. Li, Ceram. Int. **46**, 212 (2020)
4. F. Wan, X.J. Bai, K.K. Song, J.B. Zheng, X. Lin, C.D. Cao, J. Mater. Sci. Technol. **33**, 1061 (2017)
5. T. Kimura, G. Lawes, T. Goto, Y. Tokura, A.P. Ramirez, Phys. Rev. B **71**, 224425 (2005)
6. K. Noda, S. Nakamura, J. Nagayama, H. Kuwahara, J. Appl. Phys. **97**, 10C103 (2005)
7. N.R. Qu, Z.P. Li, J. Supercond. Nov. Magn. **31**, 2869 (2018)
8. M.M. Wang, R.M. Wang, H.Y. Dai, T. Li, Y. Sun, D.W. Liu, F.F. Yan, X.B. Xing, Ceram. Int. **48**, 3685 (2022)
9. L.L. Xu, J.L. Meng, Q.S. Liu, J. Meng, X.J. Liu, H.J. Zhang, Phys. Chem. Chem. Phys. **22**, 4905 (2020)
10. P. Pant, H. Agarwal, S. Bharadwaj, M.A. Shaz, J. Mater. Sci.: Mater. Electron **33**, 18871 (2022)
11. A. Ahmed, D. Mazumdar, K. Das, I. Das, J. Magn. Magn. Mater. **551**, 169133 (2022)
12. F. Bzour, A. Gismelseed, I.Z. Al-Yahmadi, F. Al-Ma'Mari, A. Al-Rawas, S. Al-Harthi, A. Yousif, H. Widatallah, M. ElZain, M.T.Z. Myint, Hyperfine Interact. (2021). https://doi.org/10.1007/s10751-021-01782-y
13. P. Tiwari, M. Yadav, A. Bastia, G.C. Pandey, C. Rath, New J. Chem. **45**, 22396 (2021)
14. A. Pal, P. Murugavel, J. Appl. Phys. **123**, 234102 (2018)
15. T. Tajiri, H. Deguchi, M. Mito, A. Kohno, J. Phys. Chem. C **125**, 14474 (2021)
16. Y. Romaguera-Barcelay, S. Talu, R.S. Matos, R.M.P.B. Oliveira, J.A. Moreira, J.P. Cruz, H.D.F. Filho, Appl. Sci. **11**, 3886 (2021)
17. G.Q. Zhang, S.J. Luo, S. Dong, Y.J. Gao, K.F. Wang, J.M. Liu, J. Appl. Phys. **109**, 07D901 (2011)
18. J.A. Dean, *Lange's Handbook of Chemistry*, 15th edn. (McGraw-Hill, New York, 1999), p.4.30-4.43
19. D.J. Keeble, S. Singh, R.A. Mackie, M. Morozov, S. McGuire, D. Damjanovic, Phys. Rev. B **76**, 144109 (2007)
20. S.X. Jin, P. Zhang, E.Y. Lu, L.P. Guo, B.Y. Wang, X.Z. Cao, Acta Mater. **103**, 658 (2016)

21. H.Y. Dai, F.J. Ye, T. Li, Z.P. Chen, X.Z. Cao, B.Y. Wang, Ceram. Int. **45**, 24570 (2019)
22. F.Z. Huang, X.M. Lu, Z. Wang, W.W. Lin, Y. Kan, H.F. Bo, W. Cai, J.S. Zhu, Appl. Phys. A **97**, 699 (2009)
23. X.L. Wen, Z. Chen, E.H. Liu, X. Lin, C.L. Chen, J. Alloy. Compd. **678**, 511 (2016)
24. Y. Tang, Y. Zhang, P.Y. Du, W. Deng, J. Am. Ceram. Soc. **96**, 2537 (2013)
25. W.N. Ge, A. Rahman, H.R. Cheng, M. Zhang, J.D. Liu, Z.M. Zhang, B.J. Ye, J. Magn. Magn. Mater. **449**, 401 (2018)
26. M.F. Zeng, Y.D. Wang, Q. Liu, X. Yuan, S.F. Zuo, R.K. Feng, J. Yang, B.Y. Wang, C.Z. Qi, Y. Lin, A.C.S. Appl, Mater. Inter. **8**, 33157 (2016)
27. W. Brandt, R. Paulin, Phys. Rev. B **5**, 2430 (1972)
28. H.Y. Dai, F.J. Ye, Z.P. Chen, T. Li, D.W. Liu, J. Alloys Compd. **734**, 60 (2018)
29. D.D. Wang, N. Qi, M. Jiang, Z.Q. Chen, Appl. Phys. Lett. **102**, 042407 (2013)
30. M.H. Ghozza, I.S. Yahia, J. Mater. Sci.: Mater. Electron. **32**, 11628 (2021)
31. Y.N. Zhang, J.J. Li, Z.Q. Zhang, F.Y. Liu, X.D. Zhao, X.Y. Liu, Chem. Res. Chin. Univ. **31**, 699 (2015)
32. M.M. Wang, H.Y. Dai, T. Li, J. Chen, F.F. Yan, R.Z. Xue, X.B. Xing, D.Y. Chen, T.D. Ping, J.J. He, Mater. Sci.: Mater. Electron. **32**, 27348 (2021)
33. K. Yadagiri, R. Nithya, S. Neeraj, A.T. Satya, AIP Adv. **7**, 035003 (2017)
34. T. Li, H.F. He, T. Zhang, B. Zhao, Z.Q. Chen, H.Y. Dai, R.Z. Xue, Z.P. Chen, J. Alloys Compd. **684**, 315 (2016)
35. L. Ni, X.M. Chen, Appl. Phys. Lett. **91**, 122905 (2007)
36. N. Ikeda, H. Ohsumi, K. Ohwada, K. Ishii, T. Inami, K. Kakurai, Y. Murakami, K. Yoshii, S. Mori, Y. Horibe, H. Kito, Nature **436**, 1136 (2005)
37. H.Y. Dai, T. Li, Z.P. Cen, D.W. Liu, R.Z. Xue, C.Z. Zhao, H.Z. Liu, N.K. Huang, J. Alloys Compd. **672**, 182 (2016)